IEEE Access
Multidisciplinary | Rapid Review | Open Access Journal

Received 24 April 2024, accepted 16 June 2024, date of publication 1 August 2024, date of current version 13 August 2024.

Digital Object Identifier 10.1109/ACCESS.2024.3436856

RESEARCH ARTICLE

An Inverted-L Monopole Array With High Beam Coverage for Antenna-in-Package Modules at the 151.5–164 GHz Band

ALBERTO HERNÁNDEZ-ESCOBAR[1,2], TAKASHI TOMURA[2], (Member, IEEE), RYOSUKE HASABA[3], (Member, IEEE), HIROSHI TANEDA[4], AND ISSEI WATANABE[5]

[1]Telecommunication Research Institute (TELMA), E.T.S. Ingeniería de Telecomunicación, Universidad de Málaga, 29010 Málaga, Spain
[2]Department of Electrical and Electronic Engineering, Tokyo Institute of Technology, Tokyo 152-8550, Japan
[3]Panasonic Industry Co., Ltd., Kanagawa 224-8539, Japan
[4]Shinko Electric Industries Company Ltd., Nagano 381-0014, Japan
[5]National Institute of Information and Communications Technology, Tokyo 184-8795, Japan

Corresponding author: Takashi Tomura (tomura@ee.e.titech.ac.jp)

This work was supported in part by the Ministry of Internal Affairs and Communications, Japan, under Grant JPJ000254; and in part by European Union under Program Horizon Europe Marie Skłodowska-Curie Actions under Grant 101110031.

ABSTRACT An inverted-L monopole radiating element is proposed for antenna-in-package modules at the 151.5-164 GHz band. Its radiation pattern is half-isotropic and is well-suited for phased arrays for mobile communications. The ideal inverted-L monopole is analyzed and initial design parameters are found. A radiating element structure designed for planar technology is proposed, which consists of eight copper layers and is fed by a stripline. Impedance matching and fabrication constraints are taken into consideration when designing the structure. An array is designed and fabricated with the same size and technology as the module. To prove its scanning capabilities, a scaled-up version of the array is fabricated and measured at 28 GHz. The beam coverage of the proposed arrays is very high, able to cover 80% with a realized gain of 10 dBi by using just 2 modules.

INDEX TERMS Antenna-in-package, antenna theory, beam steering, millimeter-wave devices, mobile antennas, phased arrays, planar arrays, radiation pattern.

I. INTRODUCTION

The ever-growing demand for high data rates and low-latency communication has driven significant advancements in wireless technology. As we progress into the era of the fifth generation of mobile communications (5G) and beyond, the exploration of millimeter-wave (mm-wave) frequencies has emerged as a promising solution to address the spectrum scarcity and accommodate the increasing traffic. For 5G, the initial focus has been on the band from 24 to 100 GHz [1]. However, regarding future perspectives, the sixth generation of mobile communications (6G) is planned to reach up to the terahertz band, from 100 GHz to 1 THz [2]. In particular, the 151.5-164 GHz band [3] has been proposed as a good candidate for very-high-capacity, short-range links [4].

The utilization of mm-wave bands in wireless communication systems introduces both opportunities and challenges. While these frequency bands offer significantly wider bandwidths, enabling the transmission of large volumes of data, they also present unique propagation challenges. At mm-wave frequencies, free-space path loss and atmospheric absorption are higher, necessitating high-gain antenna systems for enhancing signal integrity. However, in mobile communications and especially in mobile terminals, the pointing direction of the antenna cannot be fixed since the position of the device keeps changing as the user moves. Thus, the imperative for achieving beams with high gain that can dynamically scan becomes apparent. To tackle this problem, reconfigurable antennas are proposed and, among

The associate editor coordinating the review of this manuscript and approving it for publication was Debabrata K. Karmokar.

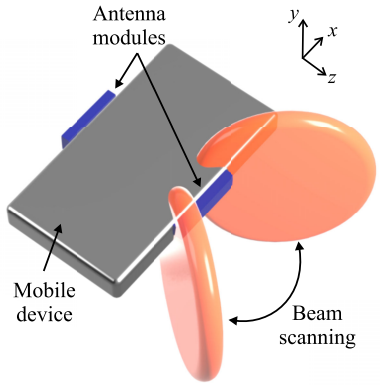

FIGURE 1. Beam coverage of two mm-wave antenna modules on a mobile device.

them, phased arrays with a large number of radiating elements are one of the most popular and convenient options, at least for the 28 GHz band [5], [6], [7], [8], [9], [10], [11], [12].

In the sub-THz band, however, there is the problem of additional circuit losses. Given the nature of mobile devices, a small-sized low-cost antenna technology is in demand. For this reason, it is relevant to use easy-to-implement fabrication procedures and, as such, planar technology is still desired for commercial applications. The use of substrate-integrated waveguide (SIW)-fed antennas [13] is one of the options to palliate the high losses. However, not only it is not clear if microstrip-like lines have such a high loss as previously expected given the current technology [14], but also SIW-fed antennas are difficult to interconnect using radio-frequency integrated circuits (RFICs). As such, antenna-in-package (AiP) solutions, this is, silicon-based modules integrated through a multilayered fabrication process with the interconnection of an RFIC, propose themselves as the best candidate [15]. This is because this technology reduces interconnection loss, makes the packaging effective, and increases manufacturing reliability.

The current goal is, then, the design of phased arrays for AiP modules that can be placed in different positions within the device to cover an even wider solid angle, as illustrated in Fig. 1, such as the one proposed in [12] for the 28 GHz band. Examples of these types of antennas in the sub-THz band are [16] and [17]. However, these works do not pay enough attention to the beam coverage, a critical figure of merit of beam-scanning antennas for mobile communications.

In phased arrays, the beam-steering capabilities are obtained only from the array factor. So, to be able to focus the beam of the array in any direction, radiation patterns with very wide shapes are usually desired: ideally, isotropic radiation. However, the presence of the mobile device itself blocks around half of the radiation, thus, making a half-isotropic radiation pattern ideal (isotropic towards half of the space, without radiation towards the other half). One of the most common radiation elements used in phased arrays is the patch [5], [11], [12], [18], [19]. However, the patch antenna has radiation nulls on the plane containing the patch, reducing end-fire radiation considerably. Other very

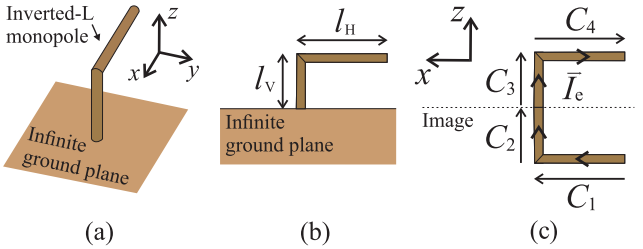

FIGURE 2. Geometry of an inverted-L monopole radiating element on an infinite ground plane. (a) 3D view. (b) Side view with dimensions. (c) Side view with integral paths.

popular elements are dipoles [7], [8], [20], or slots [6], [9]. But these radiating elements have a null in two opposite directions so, similarly, the covered angles are reduced significantly. A solution to this problem is the Huygens dipole antenna [21], [22], which has a cardioid-shaped radiation pattern. However, these elements often involve the use of intricate and electrically-small structures which would be very challenging to implement at higher frequency bands such as the one in this work.

A very simple radiating element that can produce a half-isotropic radiating pattern is the inverted-L monopole. Although not especially popular, this radiating element has been used in a wide number of applications [23], [24], [25], [26]. Furthermore, in [27], the element is proposed for phased arrays in mobile communications. However, attention is given mainly to the design for increasing its bandwidth, instead of using it for its half-isotropic radiation pattern and increased coverage. In [28], it was shown that for particular lengths of the segments of an inverted-L monopole, a half-isotropic radiating pattern can be obtained, but no practical application for this is shown.

In this contribution, an inverted-L monopole radiating element with a half-isotropic-like radiation pattern for sub-THz mobile communications is proposed. The design is carried out on the 151.5-164 GHz band. It takes into account the restrictions of commercial planar fabrication technology, proposing an array suitable for AiP modules. The novelty of the work is double. First, to the authors' knowledge and despite its simplicity, it is the first time this radiating element is used for its half-isotropic radiation pattern. Secondly, it is the first time a design is carried out from the perspective of maximizing beam coverage at the sub-THz band.

This article is organized as follows. Section II describes the operating principles of an ideal inverted-L monopole antenna. The proposed element is adapted to a realistic fabrication technology for the desired frequency band in Section III. Section IV describes a fabricated array, and compares its measured and simulated results. Coverage of the antenna modules is shown in Section V. Finally, conclusions are drawn in Section VI.

II. IDEAL INVERTED-L MONOPOLE

Firstly, to evaluate the performance of the proposed radiating element from a theoretical point of view, a very simple

inverted-L monopole, consisting only of a wire on top of a PEC plane, is studied. This means that fabrication constraints are not taken into account, and just PEC and vacuum are considered. The PEC plane will emulate the surface of the antenna module. The geometry of this inverted-L monopole antenna is plotted in Fig. 2(a). The horizontal segment of the inverted-L monopole antenna has a radiation null towards the $\pm x$ direction, but the radiation from the vertical segment has a maximum at those angles. In the same way, the vertical segment has a null in the $+z$ direction which is covered by the horizontal segment. However, the fraction of power radiated by each segment must be balanced to have a half-isotropic radiation pattern.

It is interesting to evaluate the radiation pattern of the inverted-L monopole from a coverage point of view in order to assess the design of the length of their segments. Fig. 2(b) shows the dimensions of the evaluated structure in a side view, with l_V being the vertical segment and l_H the horizontal segment of the inverted-L monopole. The thicknesses of the segments are assumed infinitesimally small, and the ground plane infinite in extension. Then, using the same analytical procedure used in [29] for the standard monopole, the value for the directivity can be found. First, using image theory, the effect of the ground plane can be taken into account, as depicted in Fig. 2(c). Then, the current passing through the monopole is assumed to be sinusoidal in the four segments as

$$\vec{I}_e(x,0,z)=\begin{cases}\hat{x}I_0\sin k_0 x, & z=-l_V, 0\le x\le l_H\\ \hat{z}I_0\sin k_0(l_H+l_V+z), & x=l_H, -l_V\le z\le 0\\ \hat{z}I_0\sin k_0(l_H+l_V-z), & x=l_H, 0\le z\le l_V\\ -\hat{x}I_0\sin k_0 x, & z=l_V, 0\le x\le l_H\end{cases} \tag{1}$$

where k_0 is the free-space wavenumber at the evaluated frequency, and I_0 is a constant that represents the maximum value of the current. Then, the electric field in any point can be computed by using

$$\vec{E}(x,y,z)\simeq -j\frac{\omega\mu_0}{4\pi}\int_C \vec{I}_e(x',y',z')\frac{e^{-jk_0R}}{R}dl' \tag{2}$$

with μ_0 the magnetic permeability of vacuum, C the path along the length of the monopole and its image (this is, $C_1+C_2+C_3+C_4$ in Fig. 2(c)), and R is $\sqrt{(x-x')^2+(y-y')^2+(z-z')^2}$. From this point on, far-field considerations are introduced in the expressions, and the electric fields spherical components, $E_\phi(\theta,\phi)$ and $E_\theta(\theta,\phi)$, can be obtained (since $E_r(\theta,\phi)\simeq 0$). Then, the directivity in any arbitrary direction (θ,ϕ) can be found by

$$D(\theta,\phi)=\frac{4\pi(|E_\theta(\theta,\phi)|^2+|E_\phi(\theta,\phi)|^2)}{\int_0^{2\pi}\int_0^{\pi/2}(|E_\theta(\theta',\phi')|^2+|E_\phi(\theta',\phi')|^2)\sin\theta' d\theta' d\phi'}. \tag{3}$$

By using (1) into (2) and (3) and resolving the integrals, it may be possible to obtain analytical expressions for the directivity. However, the mathematical complexity increases significantly very quickly and Bessel functions appear. For the sake of simplicity, in this work, the values for (3) have been obtained by solving the integrals numerically for each particular value of l_H and l_V.

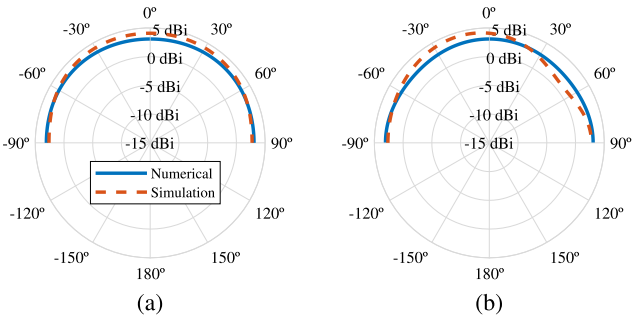

FIGURE 3. Directivity radiation patterns of the inverted-L monopole radiating element, for numerical and simulated results. (a) XZ plane. (b) YZ plane.

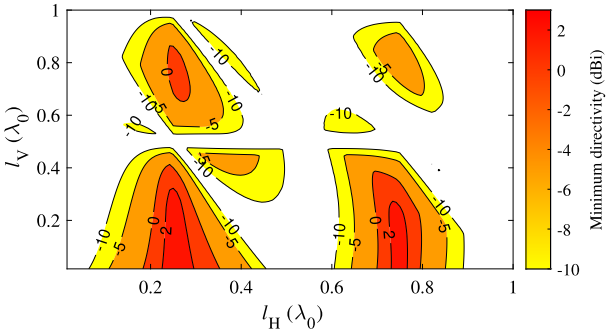

FIGURE 4. Minimum directivity of the radiation pattern for different lengths of the segments of the inverted-L monopole radiating element.

To verify the numerical results using commercial electromagnetic simulation software, the structure has been simulated using HFSS, and the directivity radiation patterns are compared in Fig. 3. The antenna dimensions are chosen as $\lambda_0/4$ for both l_H and l_V (0.4751 mm at 157.75 GHz). For the simulation of the thickness of the monopole, $\lambda_0/100$ (0.019 mm) was chosen so it is significantly thin (since analytical expressions assume zero thickness). Due to the presence of the PEC ground plane at $z=0$, there is no radiation in the $z<0$ half-space, so the expected half-isotropic value for directivity is 3 dBi. In Fig. 3, it can be seen that the radiation pattern in both simulation and numerical results show half-isotropic-like radiation patterns, with directivities ranging from 1.1 to 4.2 dBi. Differences are attributed mainly to the effect of the corner between the segments and segment coupling, which produces a slightly asymmetric pattern in the simulation.

However, the radiation pattern of the inverted-L monopole is not always half-isotropic, and it can be highly dependent on the length of its segments. A simple way of evaluating the isotropic level of the radiation of an antenna is by computing its minimum value for directivity in every direction. If the

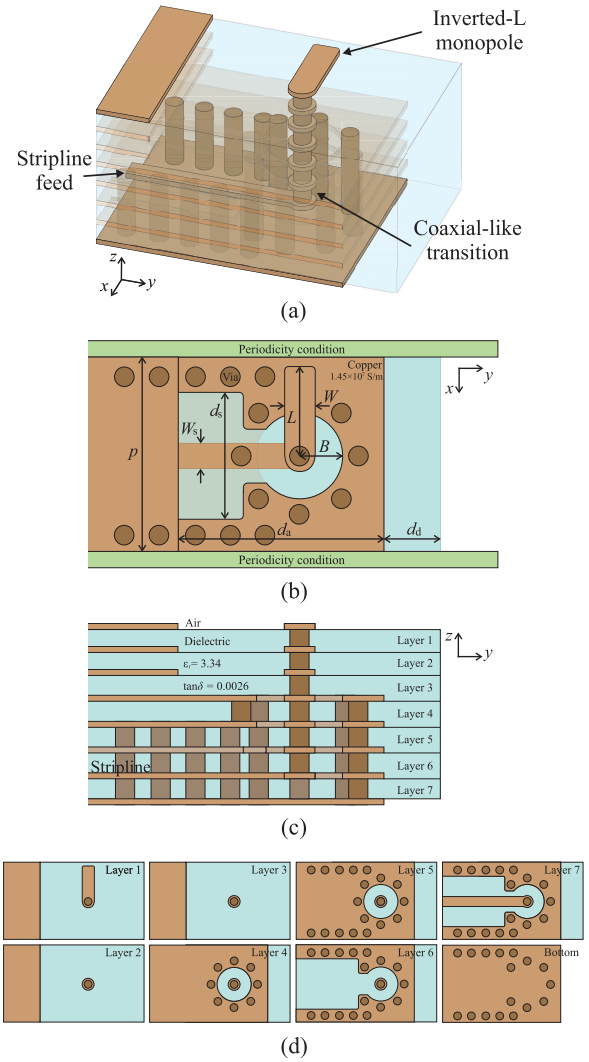

FIGURE 5. Geometry of the proposed inverted-L monopole in planar technology. (a) 3D view. (b) Top view ($d_a = 4$ mm, $d_d = 0.5$ mm, $W_s = 87$ μm, $d_s = 220$ μm, $p = 800$ μm, $B = 155$ μm, $L = 310$ μm, $W = 11$ μm). (c) Side view. (d) Top view of each layer.

minimum value is high, this means there are no nulls in any direction. It also means the maximum value is low because radiation is not being directed toward any particular direction. Using this principle and the numerical expressions obtained from (3), the minimum directivity for different combinations of l_H and l_V are obtained and plotted in Fig. 4. The highest minimum directivity is, as expected, 3 dBi, and these are the areas that correspond with the values when the radiating element has a half-isotropic radiation pattern. Thus, the segment lengths that are interesting for the design are, in particular, when l_H is around $\lambda_0/4$, and l_V is $\lambda_0/4$ or less. Of course, the lengths of the segments affect the impedance of the radiating element, so allowing flexibility can help with obtaining a better design. Furthermore, from Fig. 4 it can be seen that the radiation pattern would not change abruptly with frequency and, at least for this work's intended frequency margins, radiation would be stable if we design around the proposed values for l_H and l_V. Other regions of interest would be when $l_H \approx 3\lambda_0/4$, and $l_V < \lambda_0/4$, or when $l_H \approx \lambda_0/4$, and $l_V \approx 3\lambda_0/4$, however, for these two last cases, the size of the inverted-L monopole would be bigger, and there is no especial advantage out of them.

III. PLANAR RADIATING ELEMENT

In order to use the inverted-L monopole radiating element in AiP at 150 GHz, a simple version that can be fabricated using commercial planar technology is shown in Fig. 5. The fabrication technology used consists of copper deposition (8 layers of 20 μm thickness) and pre-preg layers as substrate (7 layers of 90 μm thickness). The dielectric used in the design and fabrication has a relative permittivity of 3.34 and loss tangent of 0.0048 at 100 GHz and the value considered for the conductivity for the copper is 1.45×10^7 S/m, one-quarter of its usual value, in order to account for copper roughness, which is significant at these frequencies. Aside from this, planar technology for these high frequencies has several limitations in terms of accuracy, dimensions, and other significant restrictions. For instance, the copper layers on the top-left corner of Fig. 5(a) are placed there to increase the amount of copper in those layers to make fabrication more stable, at the cost of antenna performance. Distance from the edge of these copper layers to the edge of the other copper layers, d_a, is 4 mm. Besides, the minimum distance from deposited copper to substrate edge, d_d, is 0.5 mm (please note that both d_a and d_d are not to scale in Fig. 5). Regarding the used vias, their diameter is 70 μm, the minimum distance between two of them is 125 μm, and the minimum distance between the edge of a via and copper-layer edge is 20 μm.

The radiating element can be divided into three parts, as shown in Fig. 5(a). First, a stripline is used to connect the element with the rest of the circuitry (layers 5-7 in Fig. 5(c)). The stripline, under layer 6, is asymmetric due to limitations in the width of the strip that could be fabricated, so the ground planes are placed under layer 7 and layer 4. Its width, W_s, is 87 μm so it has a 50 Ω impedance, and d_s is 220 μm. Second, a coaxial-like vertical transition (layers 4-6) is designed to connect the feeding stripline with the radiating part. The radius of the hole of this transition, B, was adjusted to obtain good impedance matching, and its value is 155 μm. The hole is surrounded by eight equally-distanced vias. Third and lastly, the inverted-L monopole part (layers 1-3), whose vertical part is made of a via and the horizontal part is made of a strip. The vertical part is made of three layers, resulting in a length of 250 μm ($\sim\lambda_g/4$), and the horizontal segment length, L, is 310 μm ($\sim\lambda_{\text{eff}}/4$). This follows the analytical indications from Fig. 4, although a rather high value for the vertical part was chosen to ease impedance matching. The width of the horizontal strip, W, did not have much impact on the impedance value and was left at 11 μm to keep the shape of the strip thin and uniform.

To design the radiating element for low reflection in the band, to include the effect of mutual coupling between the radiating elements of an array, primary-secondary boundaries

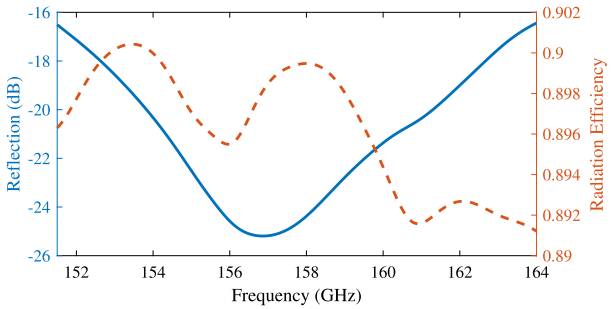

FIGURE 6. Reflection coefficient and radiation efficiency of the simulated radiating element.

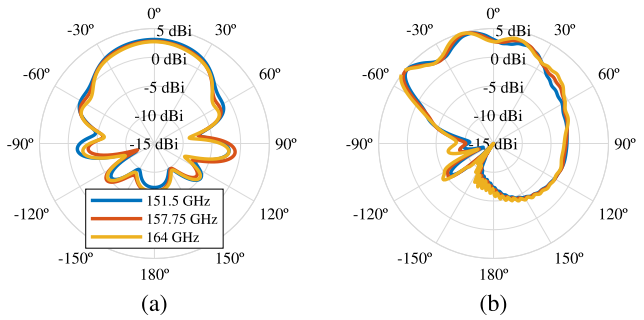

FIGURE 7. Directivity radiation pattern of the simulated radiating element at 151, 157.75, and 164 GHz. (a) XZ plane. (b) YZ plane.

were used for the design (shown in Fig. 5(b) as periodicity conditions). At these frequencies, this kind of approximation will provide accurate enough results for most cases, since the antenna module will be electrically very large compared with the size of a radiating element, and a large number of them are expected. The width of this periodicity cell, p, is 800 μm and fixes the distance between each radiating element (justified later in Section IV). Regarding the tuning of the dimensions, B and L were adjusted to obtain good impedance matching. For the vertical part of the radiating element, since it involves a discrete number of layers, it cannot be adjusted, but the cases of 2 and 4 layers were also considered. The other parameters were mainly chosen taking into account fabrication limitations and the feasibility of the structure. The radiating element as described here was simulated in HFSS, and its S_{11} parameter and radiation efficiency are shown in Fig. 6. The reflection is low, under -15 dB over the 151-164 GHz band, and the radiation efficiency is high, around 90%.

In Fig. 7, the directivity of the simulated radiating element is shown for the center and edge frequencies of the band. It can be seen that the radiation pattern is stable in frequency, however, replicating the results of half-isotropy from the ideal structure is more challenging, due to the effect of adjacent elements (some nulls in the $\pm x$ directions in Fig. 5, producing the nulls around $\pm$70-80° in Fig. 7(a)), and the blocked directions ($-y$ direction, $-$60-90° in Fig. 7(b)) by the top-left corner copper layers previously mentioned. To compensate for the lack of coverage in these directions, the radiating

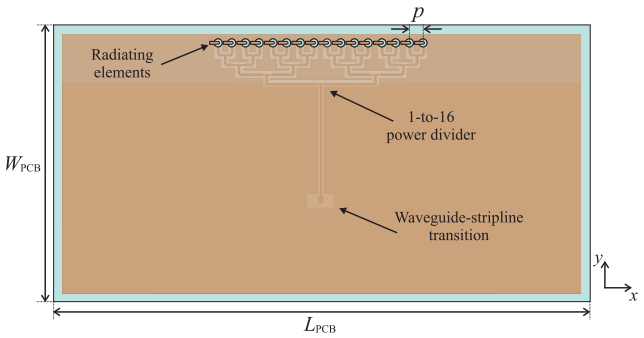

FIGURE 8. Top view of the geometry of the proposed array.

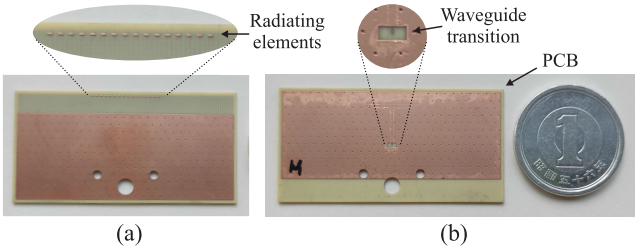

FIGURE 9. Pictures of the fabricated array. (a) Top view, zoom: radiating elements. (b) Bottom view, zoom: waveguide-stripline transition.

element was placed as close as possible to one of the edges of the module ($+y$) to cover to a certain extent some of the downward directions too (90-150° in Fig. 7(b)).

IV. ARRAY RESULTS

By using the radiating element from Section III, an array is fabricated and its results are shown here. The array is uniform and linear, and intended for building phased-array modules for mobile devices. The geometry of the proposed array is shown in Fig. 8. To take into account the effect of the whole antenna module, the array prototype is built on a PCB with length, L_{PCB}, 40 mm, and width, W_{PCB}, 20 mm. The number of elements is 16. The distance between the elements, p, is 0.8 mm. This distance has been chosen so it is slightly shorter than $\lambda_0/2$. Although using $p = \lambda_0/2$ produces overall higher values of directivity [29], end-fire radiation pattern would have two main lobes (one pointing towards $+x$ and the other towards $-x$), which would have negative consequences for communication, such as more interference and difficulties tracking the position of the base station. Besides, since there is only one beam, the gain is increased by 3 dB in the end-fire directions, which helps compensate for slightly lower gain of the radiating elements in those directions.

The proposed array was fabricated by using the technology explained in Section III, and the resulting prototype is shown in Fig. 9. Due to the lack of enough physical space on the PCB, only one-port prototypes were fabricated for the 151.5-164 GHz band. As such, beam-scanning capabilities could not be tested (but will be tested on a scaled-up version at 28 GHz). The 16 radiating elements are fed by using a 1-to-16 power divider with a tournament configuration using the same stripline as the one depicted in Fig. 5. The

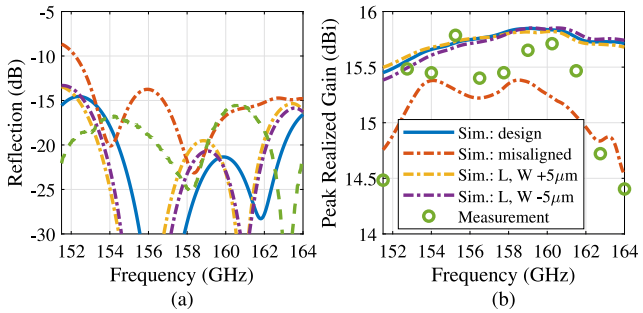

FIGURE 10. Simulated and measured results of the proposed array. (a) Reflection coefficient. (b) Maximum realized gain.

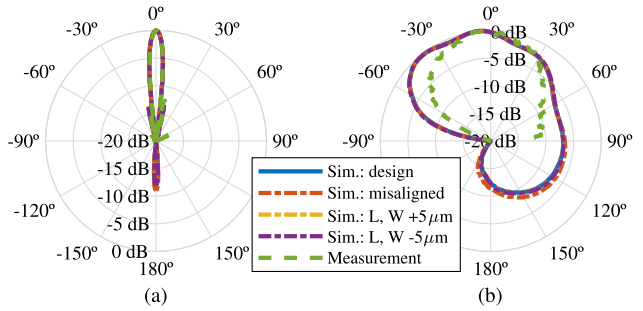

FIGURE 11. Normalized realized-gain radiation pattern of the proposed array. Simulated and measured values at 157.75 GHz. (a) XZ plane. (b) YZ plane.

PCB is connected to the measurement system by using a WR-6.5 waveguide, and a transition from this waveguide to the stripline was designed and used. Both the power divider and transition schematic can be seen in Fig. 8.

The reflection coefficient of the prototype is shown in Fig. 10(a), where the effect of the transition and power divider is included. The results show good matching over the band for both simulation and measurement. In Fig. 10(b), the realized gain over frequency is shown. At the center of the band, the realized gain is 15.8 dBi for the simulated case and 15.5 dBi for the measurement. The insertion losses of the waveguide-to-stripline transition and the power divider were accounted for by measuring a different PCB consisting of two of these structures in a back-to-back configuration. The measured gain is slightly lower than the simulated one, and even lower at the edges of the frequency band. Lastly, in Fig. 11, the normalized realized-gain radiation pattern is shown. For the fabricated case, the phase difference between the elements is 0°, thus, producing a broadside radiation pattern, as the results show. Regrettably, the measurement system only allowed measurement from $-90°$ to 90° elevation angles, however, agreement is reasonably good.

Regarding the fabrication tolerances due to the depositing procedure, after the fabrication of the prototype, two kinds of inaccuracies that could lead to performance problems were found. One is the variation in the width of the copper lines (metal pattern tolerance) and the other is the misalignment of the multiple layers. For the variation in the width of the lines, an error of up to ± 5 μm was found and some of the layers were misaligned up to ± 20 μm in the x and/or y directions.

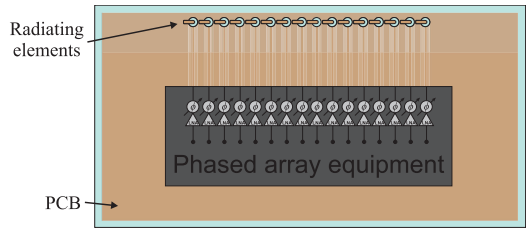

FIGURE 12. Schematic of the fabricated array at 28 GHz connected to a BBox.

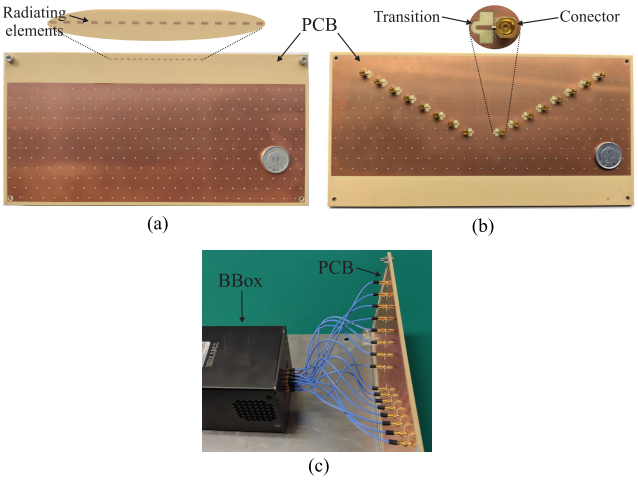

FIGURE 13. Picture of the fabricated scaled-up array for measurement at 28 GHz. (a) Top view, zoom: radiating elements. (b) Bottom view, zoom: transition and connector. (c) PCB connected to a BBox.

Three additional cases where simulated and compared with the original design and measurement results: a case with a bigger radiating element (L and W increased by 5 μm), a case with a smaller radiating element (L and W reduced by 5 μm), and a case where each layer was misaligned from the one in the top and in the bottom by 20 μm. The results of these three simulations results were also shown in Fig. 10 and Fig. 11. However, it was found out that the effect of the element size did not produce a significant variation nor for the reflection or radiation characteristics of the antenna. However, regarding the misalignment, it produced a significant change in the realized gain of the array, as shown in Fig. 10(b). Actually, the difference in the gain between the simulated and measured realized gain at the start and end of the bands could be attributed to this kind of misalignment.

To test the scanning capabilities of the array, a scaled-up version of the module PCB has been fabricated to work at 28 GHz. The size of the PCB in this case is 225.2 mm by 112.6 mm ($L_{\text{PCB}} \times W_{\text{PCB}}$). Unlike the previous prototype, in this case, the phase of each radiating element is controlled and connected to the measurement system, as illustrated in Fig. 12. To do this, each element was connected to an SMPM connector, which was connected in turn to a BBox to control the phase difference individually. BBox is a 16-channel beamforming tool that enables the feeding of 16 ports independently with variable phase and amplitude [30], and it has been used recently for mm-wave phased-array

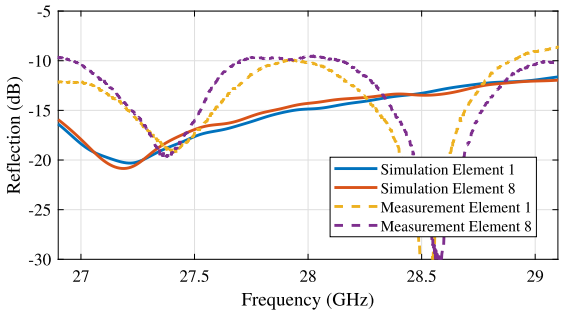

FIGURE 14. Simulated and measured reflection coefficient of the scaled-up array at 28 GHz for the first and eighth element.

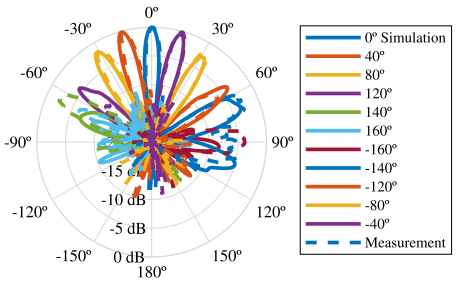

FIGURE 15. Simulated and measured normalized realized-gain radiation pattern of the scaled-up array at 28 GHz for several phase differences, XZ plane.

measurements [31], [32]. The fabricated scaled-up PCB is shown in Fig. 13.

The S_{11} parameter of the scaled-up prototype is shown in Fig. 14 over the scaled-down frequency band, which is from 26.9 GHz to 29.1 GHz. The reflection coefficient is shown for the first and eighth (starting from the left of the Fig. 12) elements of the array. The results show decent matching for both the element close to the edge (Element 1) and the central element (Element 8). By using this additional prototype, scanning could be tested, and results are shown in Fig. 15. The radiation pattern in the XZ plane is compared with simulation for several values of phase difference between the elements, as shown in the legend of the figure. Some discrepancies between simulation and measurement are found around $-90°$ and $90°$ directions due to the support system used for measurement and the presence of screws used to fix the PCB (which can be seen at the top corners in Fig. 13(a)). Despite this, it can be seen that the direction of the beam can change at a very wide angle by changing the phase difference between the elements, as expected from the XZ-plane radiation pattern of the single radiating element in Fig. 7(a).

V. COVERAGE

The main objective of the antenna module is to be able to cover as many directions as possible. A study of the covered directions is provided here. Given the number of measurements needed to provide this study in the case of the measured prototype, only results from the ideal radiating element placed on an infinite ground plane and simulation results of the fabricated prototype are provided. To calculate the coverage of the arrays, the maximum possible value of

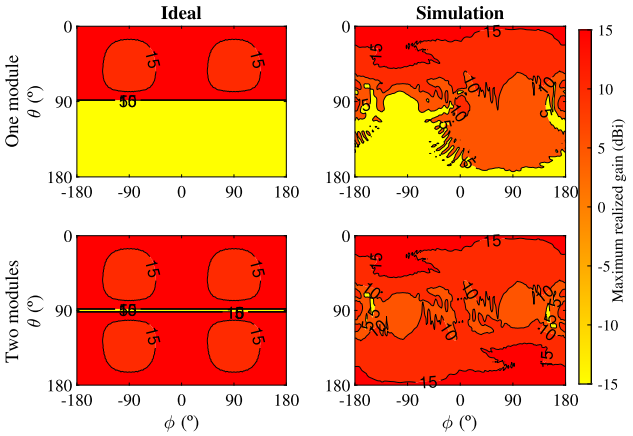

FIGURE 16. Maximum realized gain of the phased array in every direction, for the ideal and simulated cases, for one module, and for two modules facing opposite directions.

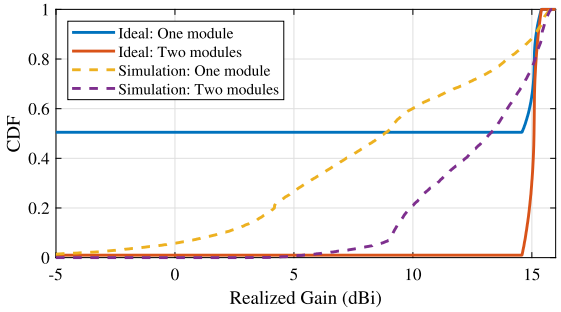

FIGURE 17. Coverage of the phased array for the ideal and simulated cases, for one or two modules.

the realized gain in every direction for each phase difference is obtained. Additionally, to increase coverage, two modules can be placed on opposite sides of the mobile device facing opposite directions, in the same way as in Fig. 1 from Section I. This maximum realized gain is shown in Fig. 16 for the ideal array and the simulated one when using one and two modules. For comparison, the cumulative distribution function (CDF) of the covered directions with at least a given amount of gain, is shown in Fig. 17. As expected, one ideal phased array can cover half of the space with a gain of around 14.6 dBi, and two of them can cover every direction except for the one of the infinite ground plane ($\theta = 90°$). In the case of the simulation of the fabricated prototype, one module can cover the 40% of directions with a gain of 10 dBi or more, while two modules could cover the 80%.

Table 1 compares the beam coverage of the proposed antenna with other mm-wave wave arrays at 28 GHz. Even after considering the effect of the higher number of elements, the proposed array performs well despite the higher frequency band. However, the improvement is more significant when compared with other works that use 3 or 4 modules, since the proposed antenna can cover a similar or higher % with just 2 modules. In the case of sub-THz arrays, no CDF or coverage efficiency study was found in the literature. However, the array proposed in [17] has a 6 dB beam coverage of $\pm 50°$ at 170 GHz, while the proposed one in this work has $\pm 74°$.

TABLE 1. Comparison with other high-coverage mm-wave arrays for mobile devices.

Reference	Radiating Element Type	Operating Band (GHz)	Array Size (λ_0^3)	Number of Modules	Elements per Module	Max. Realized Gain (dBi)	Realized Gain at 50% CDF (dBi)	Realized Gain at 20% CDF (dBi)
[33]	Quasi-Yagi	26-40	6.05×2.42×0.084	1	5	9	4.5	1.5
[18]	Patch	25.5-27.5	1.14×0.3×0.083	1	4	9.7	1	-5.5
[20]	Dipole	22-31	1.87×0.8×0.067	1	4	9.5	4	0
[26]	Inverted-L	2.41-2.5	0.45×0.45×0.033	1	2	4.12	–	–
[27]	Inverted-L	33-101	3.93×3.93×0.272	1	256	25	–	–
This work	Inverted-L	151.5-164	6.74×2.1×0.332	1	16	15.8	8.8	4.2
[19]	Patch	23.4-30	6.65×1.13×0.307	3	4	14.5	6.8	0
[6]	Slot	27-29	4×0.96×0.071	3	8	13	10.1	7.5
[9]	Slot	28-29	7.68×7.68×0.228	4	8	13.6	11.4	5.5
This work	Inverted-L	151.5-164	6.74×4.21×0.332	2	16	15.8	13.2	9.9

VI. CONCLUSION

The use of a radiation element with a half-isotropic radiation pattern in phased arrays has proven its advantages in terms of beam coverage. A very simple radiating element consisting of an L-shaped monopole has been shown to have such a radiation pattern, and a feasible implementation for it has been proposed at the sub-THz band for AiP modules.

Future research should focus on making on reducing the difference in the radiation patterns between the ideal and the implementable version to improve even further the coverage. This could be done, for example, by reducing the mutual coupling of the elements to make more stable the radiation in the directions contained in the ground plane.

An AiP prototype of a 16-element array with a power divider was fabricated and measured to measure the feasibility of the PCB fabrication process and antenna performance. The fabricated inverted-L monopole array exhibited a realized gain of 15.5 dBi and good matching over the 151.5-164 GHz band. Measurement of a scaled-up array at 28 GHz was used to prove its wide beam-scanning capabilities.

By using just two identical modules of these arrays, it is possible to cover an 80% of the directions with a realized gain of 10 dBi or more. Compared to modules that need 3 or more of them, this simplifies significantly their placement and connection within the mobile device. Due to its simplicity and half-space-covering capability, the inverted-L monopole is a very good candidate for building arrays for mm-wave mobile communications.

REFERENCES

[1] M. Shafi, A. F. Molisch, P. J. Smith, T. Haustein, P. Zhu, P. De Silva, F. Tufvesson, A. Benjebbour, and G. Wunder, "5G: A tutorial overview of standards, trials, challenges, deployment, and practice," *IEEE J. Sel. Areas Commun.*, vol. 35, no. 6, pp. 1201–1221, Jun. 2017.

[2] H. Tataria, M. Shafi, A. F. Molisch, M. Dohler, H. Sjöland, and F. Tufvesson, "6G wireless systems: Vision, requirements, challenges, insights, and opportunities," *Proc. IEEE*, vol. 109, no. 7, pp. 1166–1199, Jul. 2021.

[3] M. J. Marcus, "6G spectrum policy issues above 100 GHz," *IEEE Wireless Commun.*, vol. 28, no. 6, pp. 7–8, Dec. 2021.

[4] *ECC Recommendation*, CEPT, Gujarat, India, Apr. 2018.

[5] N. Ojaroudiparchin, M. Shen, S. Zhang, and G. F. Pedersen, "A switchable 3-D-coverage-phased array antenna package for 5G mobile terminals," *IEEE Antennas Wireless Propag. Lett.*, vol. 15, pp. 1747–1750, 2016.

[6] S. Zhang, X. Chen, I. Syrytsin, and G. F. Pedersen, "A planar switchable 3-D-coverage phased array antenna and its user effects for 28-GHz mobile terminal applications," *IEEE Trans. Antennas Propag.*, vol. 65, no. 12, pp. 6413–6421, Dec. 2017.

[7] M. Ansari, H. Zhu, N. Shariati, and Y. J. Guo, "Compact planar beamforming array with endfire radiating elements for 5G applications," *IEEE Trans. Antennas Propag.*, vol. 67, no. 11, pp. 6859–6869, Nov. 2019.

[8] F. Y. Xia, Y. J. Cheng, Y. F. Wu, and Y. Fan, "V-band wideband circularly polarized endfire multibeam antenna with wide beam coverage," *IEEE Antennas Wireless Propag. Lett.*, vol. 18, pp. 1616–1620, 2019.

[9] J. Bang and J. Choi, "A compact hemispherical beam-coverage phased array antenna unit for 5G mm-wave applications," *IEEE Access*, vol. 8, pp. 139715–139726, 2020.

[10] G. Federico, A. Hubrechsen, S. L. Coenen, A. C. F. Reniers, D. Caratelli, and A. B. Smolders, "A wide-scanning metasurface antenna array for 5G millimeter-wave communication devices," *IEEE Access*, vol. 10, pp. 102308–102315, 2022.

[11] J.-W. Kim, S.-C. Chae, H.-W. Jo, T.-D. Yeo, and J.-W. Yu, "Wideband circularly polarized phased array antenna system for wide axial ratio scanning," *IEEE Trans. Antennas Propag.*, vol. 70, no. 2, pp. 1523–1528, Feb. 2022.

[12] J. Park, A. A. Omar, J. Kim, J. Choi, B. Seong, J. Lee, and W. Hong, "Enabling spherical beam coverage for millimeter-wave stationary and mobile applications: A stackable patch antenna," *IEEE Antennas Propag. Mag.*, vol. 65, no. 3, pp. 2–14, Aug. 2022.

[13] A. Altaf, W. Abbas, and M. Seo, "A wideband SIW-based slot antenna for *D*-band applications," *IEEE Antennas Wireless Propag. Lett.*, vol. 20, pp. 1868–1872, 2021.

[14] Y. Morishita, K. Takahashi, R. Hasaba, T. Murata, K. Takinami, H. Kitamura, U. Sangawa, T. Tomura, and I. Watanabe, "Comparison between microstrip-line and substrate integrated waveguide on package substrate in 170 GHz and 300 GHz bands," in *Proc. Asia–Pacific Microwave Conf. (APMC)*, Nov. 2022, pp. 196–198.

[15] X. Gu, D. Liu, and B. Sadhu, "Packaging and antenna integration for silicon-based millimeter-wave phased arrays: 5G and beyond," *IEEE J. Microwave*, vol. 1, no. 1, pp. 123–134, Jan. 2021.

[16] S. Oh and J. Oh, "140-GHz affordable miniaturized array antenna-on-package for sub-THz transceiver," *IEEE Access*, vol. 11, pp. 132780–132791, 2023.

[17] H. Kim and J. Oh, "140-GHz wideband array antenna-in-package using multimode resonance," *IEEE Trans. Antennas Propag.*, vol. 71, no. 3, pp. 2136–2144, Mar. 2023.

[18] X. Fan and Y. Wang, "Compact millimeter-wave array with wide-angle scanning for mobile phones," *IEEE Trans. Antennas Propag.*, vol. 71, no. 8, pp. 6983–6988, Aug. 2023.

[19] X. Xia, F. Wu, C. Yu, Z. H. Jiang, R. Lu, Y. Yao, and W. Hong, "Millimeter-wave ±45° dual linearly polarized end-fire phased array antenna for 5G/B5G mobile terminals," *IEEE Trans. Antennas Propag.*, vol. 70, no. 11, pp. 10391–10404, Nov. 2022.

[20] M. M. Samadi Taheri, A. Abdipour, S. Zhang, and G. F. Pedersen, "Integrated millimeter-wave wideband end-fire 5G beam steerable array and low-frequency 4G LTE antenna in mobile terminals," *IEEE Trans. Veh. Technol.*, vol. 68, no. 4, pp. 4042–4046, Apr. 2019.

[21] W. Lin and R. W. Ziolkowski, "Theoretical analysis of beam-steerable, broadside-radiating Huygens dipole antenna arrays and experimental verification of an ultrathin prototype for wirelessly powered IoT applications," *IEEE Open J. Antennas Propag.*, vol. 2, pp. 954–967, 2021.

[22] R. Rodriguez-Cano and R. W. Ziolkowski, "Single-layer, unidirectional, broadside-radiating planar quadrupole antenna for 5G IoT applications," *IEEE Trans. Antennas Propag.*, vol. 69, no. 9, pp. 5224–5233, Sep. 2021.

[23] R. King, C. Harrison, and D. Denton, "Transmission-line missile antennas," *IRE Trans. Antennas Propag.*, vol. 8, no. 1, pp. 88–90, Jan. 1960.
[24] W. Ni and N. Nakajima, "Small printed inverted-L monopole antenna for worldwide interoperability for microwave access wideband operation," *IET Microwave, Antennas Propag.*, vol. 4, no. 11, p. 1714, 2010.
[25] S. A. Sanghai, M. Ignatenko, and D. S. Filipovic, "Low-profile two-arm inverted-L antenna design for vehicular HF communications," *IEEE Trans. Antennas Propag.*, vol. 65, no. 11, pp. 5710–5719, Nov. 2017.
[26] E. Rohadi and M. Taguchi, "Two low profile unbalanced fed inverted l elements on square conducting plane for MIMO applications," *Wireless Eng. Technol.*, vol. 5, no. 2, pp. 34–43, 2014.
[27] M. Hamza, C. L. Zekios, and S. V. Georgakopoulos, "An ultra-wideband fully-planar Inverted-L monopole (FILM) array," in *Proc. IEEE Int. Symp. Phased Array Syst. Technol. (PAST)*, Oct. 2022, pp. 1–6.
[28] A. Andãujar, J. Anguera, C. Puente, and A. Pérez, "On the radiation pattern of the L-shaped wire antenna," *Prog. Electromagn. Res. M*, vol. 6, pp. 91–105, 2009, doi: 10.2528/PIERM09012204.
[29] C. A. Balanis, *Antenna Theory: Analysis and Design*. Hoboken, NJ, USA: Wiley, 2005.
[30] TMYTEK Company. (2021). *BBox 28 GHz Datasheet*. [Online]. Available: https://www.tmytek.com/bbox
[31] W. Liu and S. Yan, "A design of millimeter-wave dual-polarized SIW phased array antenna using characteristic mode analysis," *IEEE Antennas Wireless Propag. Lett.*, vol. 21, pp. 29–33, 2022.
[32] C. Zhou, W. Yang, Q. Xue, Y. Liu, Y. Xu, and W. Che, "Millimeter-wave wideband dual-polarized LTCC antenna array based on metasurfaces for beam-scanning applications," *IEEE Trans. Antennas Propag.*, vol. 70, no. 10, pp. 9912–9917, Oct. 2022.
[33] C. Di Paola, S. Zhang, K. Zhao, Z. Ying, T. Bolin, and G. F. Pedersen, "Wideband beam-switchable 28 GHz quasi-yagi array for mobile devices," *IEEE Trans. Antennas Propag.*, vol. 67, no. 11, pp. 6870–6882, Nov. 2019.

ALBERTO HERNÁNDEZ-ESCOBAR received the B.E., M.Sc., and Ph.D. degrees in telecommunication engineering from the Universidad de Málaga, Spain, in 2014, 2016, and 2021, respectively.

In 2014, he joined the Department of Communications Engineering, Universidad de Málaga, as a Research Assistant. In 2016, he was a Granted Student with the Department of Electronic Systems, Aalborg University, Aalborg, Denmark. From September 2018 to December 2018, he was a Visiting Ph.D. Student with the Department of Electrical Engineering, KU Leuven, Belgium. Since 2022, he has been a Postdoctoral Fellow with Tokyo Institute of Technology, Japan. His research interests include the analysis, circuit modeling, design, and application of planar antennas.

Dr. Hernández-Escobar was a recipient of a Ministerio de Educacin, Cultura y Deporte Scholarship (2016–2021) and a Horizon Europe Marie Skłodowska-Curie Fellowship (2023–present).

TAKASHI TOMURA (Member, IEEE) received the B.E., M.E., and D.E. degrees in electrical and electronic engineering from Tokyo Institute of Technology, Tokyo, Japan, in 2008, 2011, and 2014, respectively.

He was a Research Fellow of Japan Society for the Promotion of Science (JSPS), in 2013. From 2014 to 2017, he was with Mitsubishi Electric Corporation, Tokyo, and was engaged in the research and development of aperture antennas for satellite communications and radar systems. From 2017 to 2019, he was a Specially Appointed Assistant Professor with Tokyo Institute of Technology, Tokyo, where he is currently an Assistant Professor. His research interests include electromagnetic analysis, aperture antennas, and planar waveguide slot array antennas. He is a member of the IEICE. He received the Best Student Award from Ericsson Japan, in 2012, the IEEE AP-S Tokyo Chapter Young Engineer Award, in 2015, the Young Researcher Award from IEICE Technical Committee on Antennas and Propagation, in 2018, and the IEEE MTT-S Japan Chapter Young Engineer Award, in 2022.

RYOSUKE HASABA (Member, IEEE) received the B.E. and M.E. degrees in electrical and electronic engineering from Tokyo Institute of Technology, Tokyo, Japan, in 2009 and 2012, respectively. In 2012, he joined the Core Technology Development and Research Center, Panasonic Corporation, Yokohama, Japan. Since 2012, he has been involved in research on wireless power transfer. He is currently with Panasonic Industry Company Ltd., and engages in development of antennas. He is a member of the IEICE. He received "Young Engineer Award" and "Uenohara Michiyuki Memorial Award" from IEEE MTT-S Japan Chapter, in 2020, "the Best Industry Paper" from IEEE Wireless Power Transfer Conference, in 2021, and "Best Poster Award (Second)" from IEEE International Symposium on Antennas and Propagation, in 2023.

HIROSHI TANEDA received the B.E. degree in materials science and engineering from the National Institute of Technology (NIT), in 2009, and the M.E. degree in materials science and engineering from Nara Institute of Science and Technology (NAIST), Miyazaki, Nara, Japan, in 2011.

Since 2011, he has been with Shinko Electric Industry, Nagano, Japan. He is currently the development of build-up process for semiconductor package substrates. He specializes in build-up substrates, bendable substrates, glass core substrates, and lithography.

Mr. Taneda received the Best Paper Award at the 28th Microelectronics Symposium, in 2018.

ISSEI WATANABE received the B.E., M.E., and Ph.D. degrees in engineering science from Osaka University, in 1999, 2001, and 2005, respectively.

From 2001 to 2004, he worked on growth of epitaxial heterostructure by MBE and fabrication and characterization of cryogenically cooled InGaAs/InAlAs HEMTs. In 2004, he joined the National Institute of Information and Communications Technology (NICT), Tokyo, Japan, where he has been engaged in the research and development of nanoscale gate compound semiconductor HEMTs and MMICs and high-frequency measurement technology for millimeter- and terahertz-wave applications.

Dr. Watanabe is a member of Japan Society of Applied Physics (JSAP) and the Institute of Electronics, Information and Communication Engineers (IEICE).